Surface Air-Pressure Measurements from Space Using Differential Absorption Radar on the right wing of the 60GHz oxygen band

A. Battaglia[1,2], **E. Rumi**[3], **R. Reeves**[3], **I. Sikaneta**[4], **S. D'Addio**[4]

[1]Dipartimento di Ingegneria dell'Ambiente, del Territorio, Politecnico di Torino, Turin, Italy
[2]Department of Physics and Astronomy, University of Leicester, Leicester, United Kingdom
[3]Rutherford Appleton Laboratory, UKRI, STFC, Harwell-Oxford Campus, Didcot, United Kingdom
[4]ESA-ESTEC, Noordwijk, Netherlands

Key Points:

- Differential absorption radars with multiple tones within the oxygen band to enable surface pressure measurements with few hPa accuracy
- Cloud, rain and water vapour produce biases in the surface pressure that must be corrected
- Errors can be minimized by adopting tunable frequencies and frequency diversity.

Corresponding author: Alessandro Battaglia, `alessandro.battaglia@polito.it`

Abstract

Surface Air-pressure is one of the most important parameters used in Numerical Weather Prediction (NWP) models. Although it has been measured using weather stations on the ground for many decades, the numbers of measurements are sparse and concentrated on land. Global measurements can only be achieved by using remote sensing from Space, which is challenging; however, a novel design using Differential Absorption Radar (DAR) can provide a potential solution. The technique relies on two facts: firstly the electromagnetic fields are absorbed mainly by two atmospheric components the oxygen and water vapour, and secondly that oxygen is well mixed in the atmosphere. In this work we discuss a space-borne concept, which aims at providing near global, consistent, and regular observations for determining surface air pressure from space by a design of a multi-tone radar operating on the upper wing of the O_2 absorption band with tones from 64 to 70 GHz. Simulations of radar vertical profiles based on the output of a state of-the-art microphysical retrievals applied to the A-Train suite of sensors are exploited to establish the performance of such a system for surface pressure determination. In particular the identification and quantification of errors introduced by the presence of water vapour, cloud liquid water and rain water and the potential of a correction via the three-tone method is discussed. Results show that accuracies of the order of few hPa are at reach.

1 Introduction

Surface Air-pressure is one of the most important parameters used in Numerical Weather Prediction (NWP) models. It has long been recognized that measurements of surface pressure are of critical importance in assessing the current state of the atmosphere and oceans as well as in forecasting their future evolution. Currently, surface pressure data are available from land-based weather monitoring stations which are supplemented over the oceans by reports from ships and buoys. The coverage of the land-based network is highly in-homogeneous and 90% of stations are on land and concentrated on the Northern Hemisphere. Coverage over oceans is very sparse. Global measurements can only be achieved by remote sensing from space, which is challenging. However, a novel design by RAL space using Differential Absorption Radar (DAR) with multiple tones within the right wing of the oxygen band can provide potential solution. Electromagnetic waves are absorbed in the atmosphere as a function of frequency. In the microwave region, two compounds are primarily responsible for the majority of signal absorption: oxygen (O_2) and water vapour (H_2O) as illustrated in Fig. 1 for frequencies below 125 GHz. Two absorption peaks are present in this region: one at 22 GHz due to water vapour and a second and third one at 60 GHz and 118 GHz due to oxygen.

Historically cloud radars have been used with frequencies in atmospheric windows. More recently differential absorption radars (DAR) have been proposed as well with frequency operating in absorption bands. The 183 GHz water vapor absorption band has been proposed for DAR to retrieve water vapour (Lebsock et al., 2015; Millán et al., 2016; Battaglia & Kollias, 2019; Battaglia et al., 2020) and the JPL Vapour In-cloud Profiler Radar) (VIPR). The VIPR system has provided a proof of concept (Roy et al., 2018, 2020). Similarly Active Microwave Air Pressure Sounders (AMAPS) have been proposed adopting multiple tones selected inside the 60 GHz and 118 GHz oxygen bands (Flower & Peckham, 1978; Millán et al., 2014; Lin & Min, 2017; Lin et al., 2021); since oxygen is a well mixed gas in the atmosphere therefore the total attenuation of the column is a proxy to the surface pressure.

Differential absorption measurements of two tones, one in the oxygen band and another off the band using pulse radar enable surface pressure measurements, with measurements of additional tones achieving improved accuracy. The particular advantage of microwave over optical radiation is its ability to penetrate clouds. However, clouds

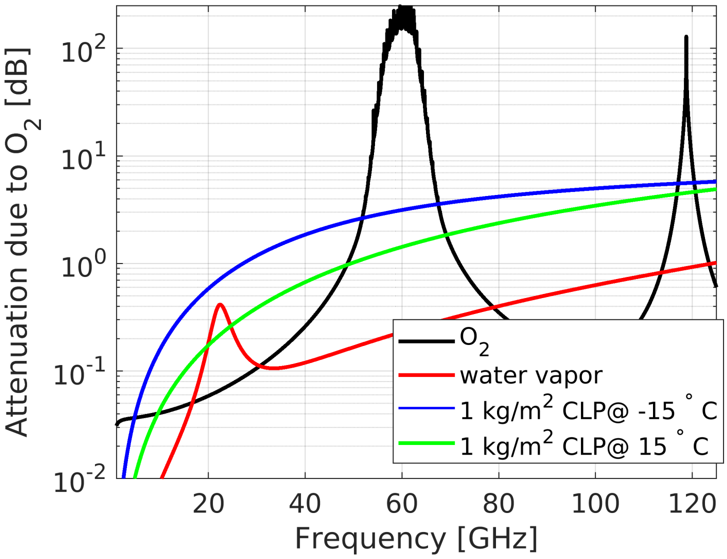

Figure 1. Nadir optical thickness contribution of O_2, water vapor and a cloud liquid path of $1\,\mathrm{kg/m^2}$ at -15 and +15°C in the microwave region between 1 and 125 GHz for the U.S. standard atmosphere.

do absorb millimetre waves and both the degree of absorption and its variation with frequency affects the system design and therefore the accuracy of the retrieval of surface air pressure (Flower & Peckham, 1978). The same applies to water vapour. Temperature dependent pressure broadening occurs in the oxygen band which affects the line profile. Therefore the AMAPS concept must be supported by the use of a multi-spectral Microwave Radiometer in order to provide measurements for temperature and water vapour profiles. Identification, quantification and correction of errors introduced by the presence of water vapour, cloud liquid water and rain water will enhance accuracy of pressure measurements. Adopting a tuneable frequency band for the in-band tone will support minimisation of errors. Fnally, implementation of frequency diversity will increase the total number of independent samples to increase accuracy.

In this work we propose a space-borne concept based on the design of a multi-tone radar operating on the upper wing of the O_2 absorption band with tones from 64 to 70 GHz. The theory underpinning the concept is outlined in Sect. 2. Then error budget and sources of uncertainties are thoroughly discussed (Sect. 3). Simulations of radar vertical profiles based on the output of a state-of-the-art microphysical retrievals applied to the A-Train suite of sensors are exploited to establish the performance of a space-borne system for surface pressure determination (Sect. 4). Conclusions and recommendations are drwan in Sect. 5.

2 Background theory

The surface peak return for a nadir incidence radar with a Gaussian circular antenna and for a homogeneous surface with surface normalised backscattering cross section σ_0, and height of r can be written as (Lin & Hu, 2005; Battaglia et al., 2017):

$$P_r(f) = \underbrace{P_t \frac{G_0^2 \lambda^2 \theta_{3dB}^2}{2^9 \pi^2 \log(2) l_{tx} l_{rx}}}_{C(f)} \frac{T^2(f)\sigma_0(f)}{r^2} = C(f) \frac{\pi^5 |K_W|^2}{\lambda^4} c\tau_p \frac{Z_{surf}(f)}{r^2} \tag{1}$$

where G_0 is the antenna gain along the boresight, θ_{3dB} is the antenna 3 dB beamwidth, l_{tx} and l_{rx} are the loss between the antenna and receiver port and between the transmitter and the antenna port, respectively, $C(f)$ is the radar constant, K_W is the dielectric factor of water ($|K_W|^2$ is assumed to be 0.93 throughout this paper), τ_p is the pulse length, $T(f)$ is the the atmospheric transmittance at the radar wavelength (lambda) caused by precipitation, cloud liquid water, water vapor and gases:

$$T(f) = e^{-\tau_{rain} - \tau_{cloud} - \tau_{O_2} - \tau_{wv}} \tag{2}$$

where we have separated the contributions of the different components to the optical thickness τ. In the right hand side of Eq.(1) Z_{surf} is the surface peak reflectivity (expected value without noise). For instance the optical thickness due to O_2 can be written as:

$$\tau_{O_2}(f) = \alpha_{O_2}(f) C_{O_2} = 0.232 \alpha_{O_2}(f) \frac{p_{surf}}{g} \tag{3}$$

where C_{O_2} is the columnar O_2 content per unit surface in kg/m^2 and α_{O_2} is the absorption coefficient per unit mass (see example in Fig. 2, left y-axis). The corresponding optical thickness for a standard atmosphere is shown in the right axis of Fig. 2. Note that for frequencies between 54.6 and 65 GHz τ_{O_2} exceeds 5 (therefore causing two-way path integrated attenuation (PIA) larger than 43.43 dB).

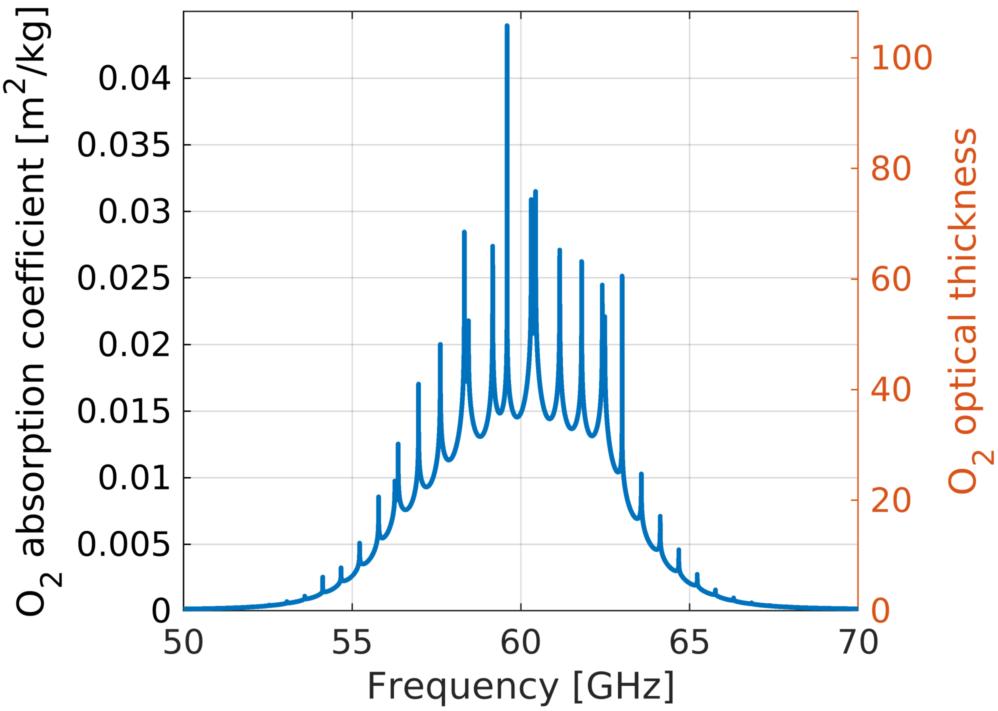

Figure 2. Average O_2 mass absorption coefficient (left axis) or equivalently O_2 total atmospheric optical thickness (right axis) for frequencies across the oxygen absorption band based on a US standard atmosphere profile. Right panel: optical thickness due to O_2 as a function of the frequency based on a standard atmosphere profile. The absorption model is based on the model Liebe et al. (1992) with the line width $1/T$ temperature dependence proposed by Schwartz (1998).

Because of the exponential dependence of pressure in the Earth's atmosphere the optical thickness is generally completely saturated within the troposphere and certainly has its biggest contribution in the levels closed to the ground. The column O_2 amount is proportional to the column air mass, C_{air}, via the O_2 mass mixing ratio of O_2 to total air (equal to 0.232) . Since $C_{air} = \frac{p_{surf}}{g}$, Eq. 1 can be rewritten as:

$$P_r(f) = \frac{C(f)\sigma_0(f)}{r^2} e^{-2\tau_{O_2} - 2\tau_{rain} - 2\tau_{cloud} - 2\tau_{wv}} = \frac{C(f)\sigma_0(f)}{r^2} e^{-0.464\, \alpha_{O_2} \frac{p_{surf}}{g} - 2\tau_{rain} - 2\tau_{cloud} - 2\tau_{wv}} \tag{4}$$

When two radar tones, the inner band frequency, f_i, and the outer band frequency, f_o, are used, then the ratio of the radar received powers from these two channels is

$$\frac{P_r(f_i)}{P_r(f_o)} = \frac{C(f_i)}{C(f_o)} \frac{\sigma_0(f_i)}{\sigma_0(f_o)} e^{-2\Delta\tau_{O_2}} e^{-2\Delta\tau_{rain} - 2\Delta\tau_{cloud} - 2\Delta\tau_{wv}} \tag{5}$$

where $\Delta\tau_{O_2}(f_i, f_o) \equiv \tau_{O_2}(f_i) - \tau_{O_2}(f_o)$ and similarly for the other Δ quantities. The ratio in Eq. 5 is predominantly driven by the surface atmospheric pressure, with the details of the temperature and pressure profiles having secondary influences on effective O_2 absorption coefficients in Eq. 5.

Rearranging Eq. (5) by using Eq. (1) we find:

$$10 \log_{10} \left[\frac{Z_{surf}(f_i)}{Z_{surf}(f_o)} \frac{f_i^4}{f_o^4} \frac{\sigma_0(f_o)}{\sigma_0(f_i)} \right] = -\Delta_2 PIA_{O_2}(f_i,\, f_o) - \Delta_2 PIA_{hydro}(f_i,\, f_o) - \Delta_2 PIA_{wv}(f_i,\, f_o) \tag{6}$$

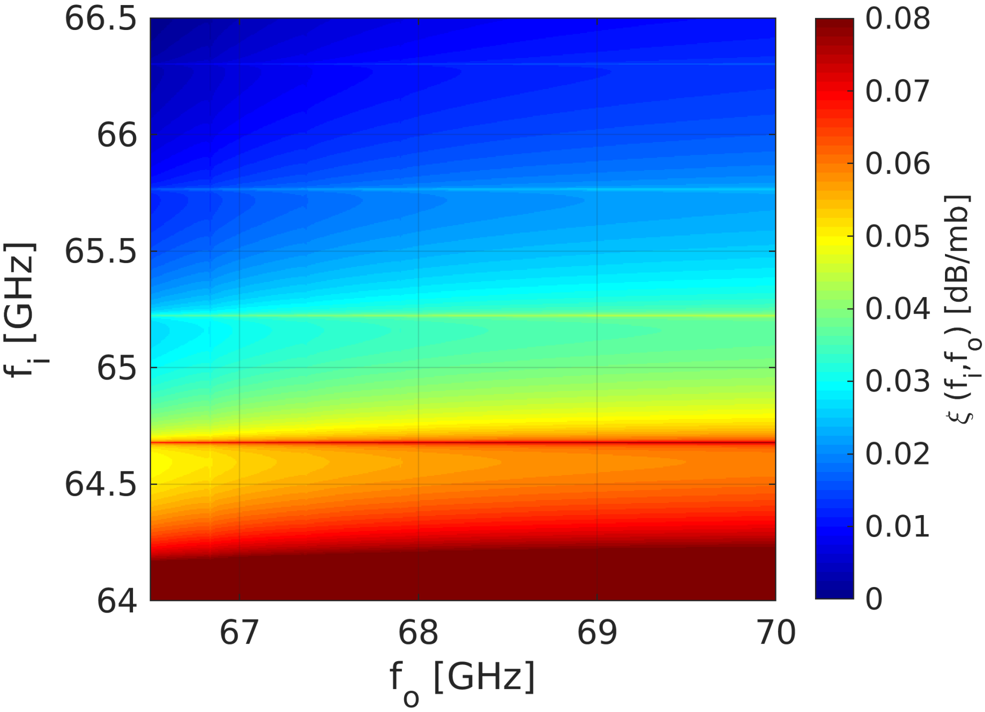

Figure 3. Sensitivity of the differential surface radar return to the surface pressure for a U.S. Standard Atmosphere for pairs of frequencies in the upper wing of the O_2 60 GHz line.

where the same pulse length has been assumed for all tones and where $\Delta_2 PIA$ indicates the 2-way differential path integrated attenuation (i.e. $\Delta_2 PIA(f_i, f_o) \equiv 2[PIA(f_i) - PIA(f_o)]$) expressed in dB with the subscripts indicating the source of the attenuation. Eq. (6) can be used to invert for $\Delta_2 PIA_{O_2}(f_i, f_o)$; then by using Eq. (3) it can be seen that there is a very simple near-linear relationship between surface air pressure and the surface reflectivities measured in dBZ at frequencies f_i and f_o, i.e.:

$$p_{surf} = \frac{\Delta Z_{surf}(f_o,\, f_i) - \Delta\sigma_0(f_o, f_i) + 40\log_{10}\left[\frac{f_o}{f_i}\right] + \Delta_2 PIA_{hydro}(f_o,\, f_i) + \Delta_2 PIA_{wv}(f_o,\, f_i)}{\xi(f_i,\, f_o)} \tag{7}$$

where we have introduced the surface reflectivity sensitivity to surface pressure for the given pair of frequencies, f_i and f_o:

$$\xi(f_i,\, f_o) \equiv \frac{\alpha_{O_2}(f_i) - \alpha_{O_2}(f_o)}{0.4962\, g} \tag{8}$$

This quantity is shown for the 60 GHz upper wing within the region of not overwhelming absorption in Fig. 3. Note that the maximum sensitivity is typically reached when there is maximum separation between the two frequencies and that for this range of frequencies never exceeds 0.06 dB/hPa.

3 Error budget for pressure measurements

It is important to review and assess all the error sources involved in determining surface air-pressure from Eq. (7). With ESA funded feasibility study RAL Space proposed a a space-borne system design options as shown in Tab. 1. These specifics will be used as a reference. All different error sources associated to each one of the terms present in the numerator and the denominator of Eq. (7) will now be discussed. The total error can be computed assuming that the different error sources are independent.

3.1 Uncertainties in surface differential reflectivity measurements

The first error is associated with ΔZ_{surf}, the surface differential reflectivity. Because what matters in the derivation of p_{surf} is only the difference in surface reflectivities no biases will arise from miscalibration of the two channels as far as the two channels are properly cross-calibrated. Any relative miscalibration between the two channels will of course produce a bias in the surface pressure estimation.

Let's us now consider the random errors associated to noisiness of reflectivity measurements. If we differentiate Eq. (5) and by following the derivation in Appendix A for the estimate of the noise subtracted signal (Eq.19) the error induced in the surface pressure is:

$$\delta p_{surf} = \frac{\delta\Delta Z_{surf}(f_o, f_i)}{\xi(f_i,\, f_o)} = \frac{4.343}{\xi(f_i,\, f_o)}\sqrt{\frac{1}{N_i}\left(1+\frac{1}{SNR(f_i)}\right)^2 + \frac{1}{N_o}\left(1+\frac{1}{SNR(f_o)}\right)^2} \tag{9}$$

where $SNR(f)$ is the single pulse signal to noise ratio of the surface return at the given frequency and N_i and N_o are the number of independent samples collected at the inner and outer frequency. In formula (9) there are two counteracting effects: if we select f_i close to the absorption peak then the sensitivity $\xi(f_i, f_o)$ becomes larger, thus suppressing the error but simultaneously $SNR(f_i)$ becomes small, thus increasing the argument of the square root.

Consider a level of SNR_o for the surface return at the outer frequency. Since in that case the attenuation of the O_2 can be assumed negligible such value is driven by the system design and the possible presence of cloud/rain/water vapor. Then it is possible to assess which is the optimal selection of f_i and f_o that minimize the error in p_{surf} under the assumption that a given amount of total power is transmitted by the radar but that the power can be different in the outer compared to the inner tone. The result of the minimization process is illustrated in Fig. 4. For $f_o = 70$ GHz or above the optimal inner frequency is typically between 64.3 and 65.5 GHz depending on SNR_o (different coloured curves as indicated in the legend). Note that the behaviour of the curves

Table 1. Instrument baseline design specifications with a “pressure” and “cloud” mode (see text in Sect.4.4 for details).

DAR Instrument	“pressure” mode	“cloud” mode
TX power	1 kW	
Frequencies	65-66, 70 GHz	70 GHz
Antenna diameter	2 m	
Altitude	500 km	
Pulse width	1.0 μ s	3.3 μ s
Bandwidth	1000 kHz	300 kHz
PRF	6 kHz	
System losses	2 dB	
Receiver Noise Figure	5 dB	
Receiver Temperature	290 K	
Minimum detectable signal	-109.2 dBm	-114.3 dBm
10 dB surface peak power@70 GHz	-56.2 dBm	-56.2 dBm
10 dB surface peak return	49.0 dBZ	43.8 dBZ
SNR_o	52.9 dB	58.1 dB
Single pulse sensitivity@70 GHz	-3.9 dBZ	-14.3 dBZ
Footprint diameter	1.3 km	

with a lot of oscillations is associated to multiple secondary absorption lines present within the O_2 band (Fig. 2 and Fig. 1 in Lin and Min (2017)).

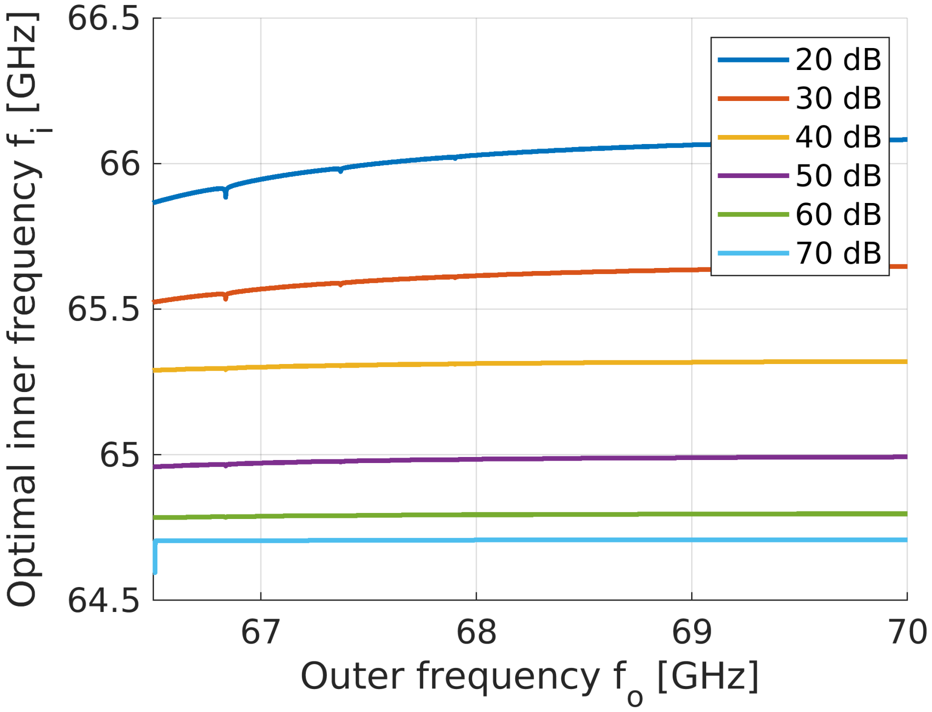

Figure 4. Optimal frequency to perform pressure DAR measurements for different levels of SNR_o for the right wing of the O_2 line.

The corresponding minimum errors computed when averaging 10^4 independent samples are plotted in Fig. 5, left panel. Clearly better results are found for high SNR_o (i.e. more sensitive radars or absence of clouds/precipitation and low water vapor contents) and when the outer frequencies is away from the center of the absorption band. In the right panel the differences in the optical thicknesses for the optimal frequency pairs are shown. With increasing SNR_o or moving away from the center of the absorption band larger $\Delta\tau$ minimize the error in the surface pressure. These findings contradict the conclusions of the study by Lin and Min (2017) who suggested that the best results are achieved when the two-way differential absorption optical depth between the inner and outer frequencies is equal to 1. In our cases $\Delta\tau$ are usually much larger than that.

3.2 Uncertainties in differential σ_0

Normalised surface backscatter cross section variation between f_i and f_o must be corrected for. For incidence close to nadir, the quasi- specular scattering theory is considered valid in the modelling of ocean surfaces. Then, the ocean surface is assumed isotropic and the surface wave distribution probability density is only a function of the surface mean-square slope, $s(v)$, according to the Fresnel approximation (Li et al., 2005):

$$\sigma_0(\theta, v, f) = \frac{|\Gamma(\theta = 0, f)|^2}{[s(v)]^2 \cos^4 \theta} \exp\left(-\frac{\tan^2 \theta}{[s(v)]^2}\right) \tag{10}$$

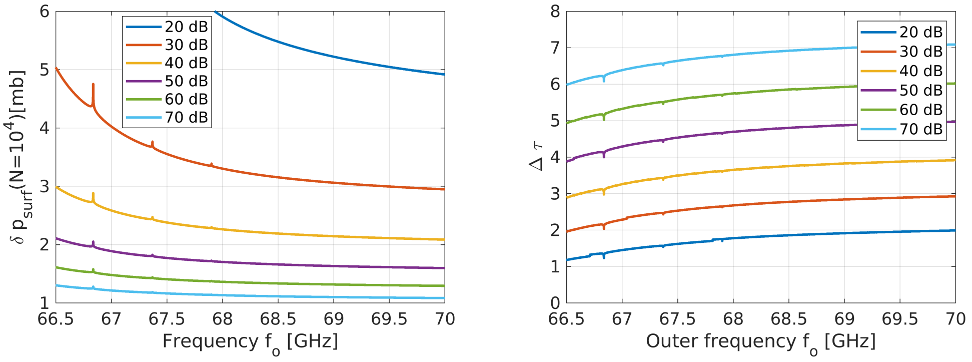

Figure 5. Left panel: minimum error associated to the noisiness of reflectivities expected in the retrieval of p_{surf} in correspondence to $N = 10^4$ independent samples. The error is computed according to formula (9) with the use of the optimal frequencies shown in Fig. 4 as a function of the outer frequency for different levels of SNR_o as indicated in the legend. Right panel: difference in τ_{O_2} in correspondence to the optimal combination of frequencies shown in Fig. 4.

where v is surface wind speed in meters per second, and $[s(v)]^2$ is the effective mean-square surface slope. The ocean surface effective Fresnel reflection coefficient at normal incidence is

$$\Gamma(\theta = 0, f) = \frac{n(f) - 1}{n(f) + 1} \tag{11}$$

where n is the frequency-dependent complex refractive index for seawater. As a result, the only dependence on the radar frequency is in the term in Eq. (11). Since the refractive index is varying gently across frequencies also this term will show a gentle variation. This is demonstrated in Fig. 6 that shows how the $\Delta\sigma_0[dB] = \sigma_0(f_i)[dB] - \sigma_0(f_o)[dB]$ between frequencies slightly depends on temperature.

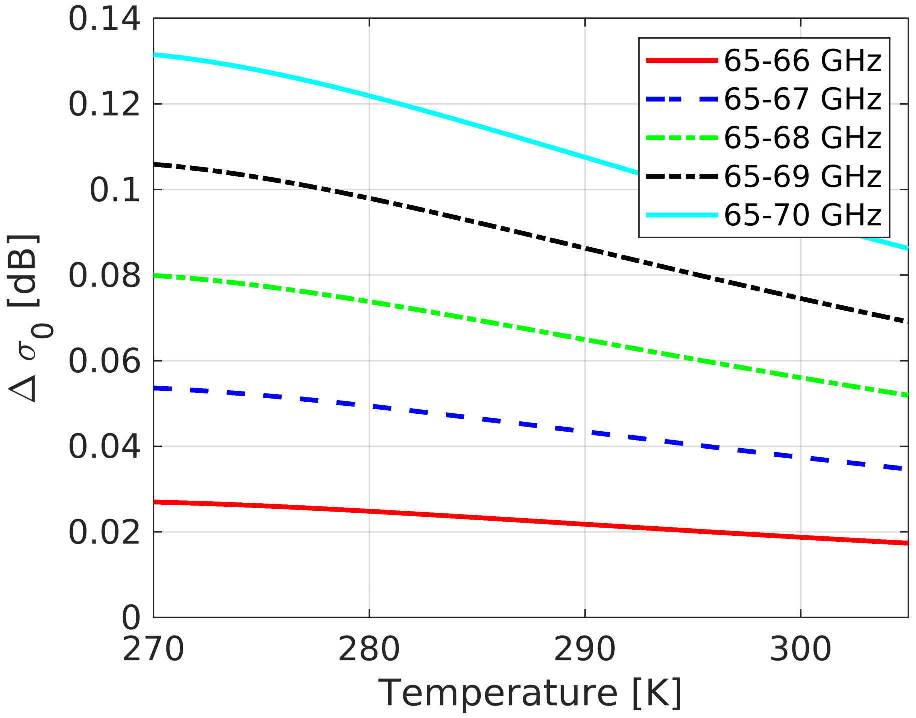

Figure 6. Difference between σ_0 values in dB when changing frequencies in the range of frequencies listed in Tab. 1 on the right wing of the O_2 absorption band.

From Eq. (7) it is clear that errors $\delta\Delta\sigma_0[dB]$ translates in errors in surface pressure according to:

$$\delta p_{surf} = \frac{\delta\Delta\sigma_0(f_o, f_i)}{\xi(f_i,\ f_o)} \tag{12}$$

Corrections for the frequency variability of σ_0 must be certainly performed but even assuming a residual 5% error on $\Delta\sigma_0$ we do not expect this error to be dominant unless separated by more than 5 GHz are adopted. For instance if 65 and 78 GHz are adopted then $\Delta\sigma_0$ is of the order of 0.3 dB; the residual error $\delta\Delta\sigma_0 = 0.015$ dB will contribute to 0.5 hPa error for pairs with $\xi = 0.03$ dB/hPa. In order to minimize this error it is recommended to keep frequencies as close as possible.

3.3 Uncertainties related to water vapor differential attenuation

Water vapor absorption tends to increase with frequency. This will introduce the differential attenuation term represented by the last term in the numerator of Eq. 7. It is important to establish to which accuracy the IWV needs to be derived from ancillary measurements (e.g. radiometer channels). A large database of temperature and water vapor profiles over ocean surfaces has been constructed. It is based on the full 2008 year of CloudSat orbits and co-located ECMWF auxiliary product. Profiles have been clustered according to classes of near surface temperature, T_{ns} (with 2.5 K binning width) and integrated water vapor, IWV (with 1 kg/m^2 binning width). The two-way path integrated differential attenuation for the pair 65 and 70 GHz are shown in Fig. 7 for $T_{ns} = 278.75$ K and $T_{ns} = 293.75$ K.

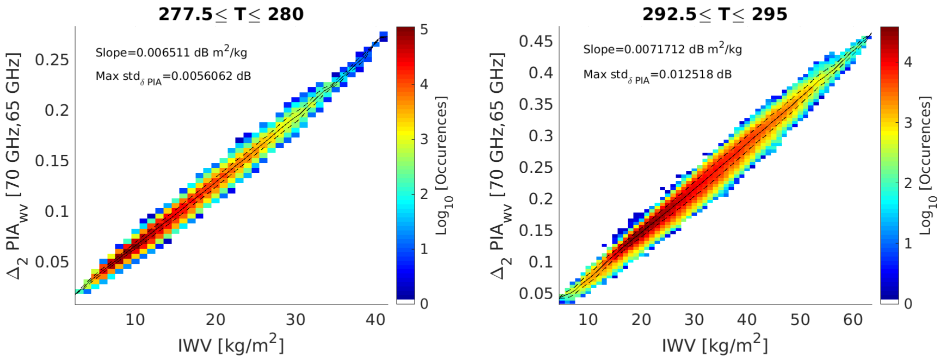

Figure 7. Density plot for the differential two-way PIAs for the 65-70 GHz pair as a function of the IWV for profiles having near surface temperatures in the range 277.5-280 K (left panel) and 292.5-295 K (right panel).

The continuous line shows the mean value whereas the dashed lines indicate the variability for any given IWV in the $\Delta_2 PIA_{wv}$ introduced by the T_{ns} and by the water vapor and temperature vertical distribution variability. In both cases such variability is less than 0.012 dB (value achieved for the warmest temperature interval with IWV=30 kg/m^2). The impact of uncertainties on the knowledge of IWV can be accounted for using the slope of the fitting to these datasets. When normalised to the frequency range a value of about 0.00135 dB m^2 kg^{-1} GHz^{-1} is found. The uncertainty in the $\Delta_2 PIA_{wv}(f_i, f_o)$ introduced by an uncertainty in IWV of δIWV, can be computed by multiplying this value by the slope value and by $f_o - f_i$. E.g. for a pair separated by 5 GHz a 3 kg/m^2 uncertainty in the IWV will propagate into an uncertainty of 0.02 dB. Depending on the targeted pressure uncertainty that is required, this analysis, combined with formula (7) allows to estimate what is the required knowledge of the IWV. As a rule of thumb uncertainties in IWV about the maximum between 2 kg/m^2 and 10% of the total IWV are required.

3.4 Uncertainties in rain and cloud differential attenuation

If clouds and rain are present in the atmosphere they cause an additional differential attenuation signal. If not accounted for, such signal could be interpreted as coming from a pressure variation, thus causing a bias. Since hydrometeor attenuation is typically increasing with frequency, in the right wing of the O_2 line, overestimating the rain/cloud amount will produce a smaller differential signal between the inner and outer frequencies, thus will produce a negative pressure bias.

Around 60 GHz attenuation is mainly caused by liquid hydrometeors. Fig. 8 shows the extinction coefficients of rain per unit mass as a function of the mean mass weighted diameters, D_m ,for two frequencies in the right wing of the 60 GHz band. For the same columnar rain water path (e.g. 1 kg/m^2) DSD with D_m around 1.5 mm produce an attenuation which is about four times (e.g. 11 dB) the attenuation caused by the cloud droplets (e.g. 3 dB) with the same mass water path.

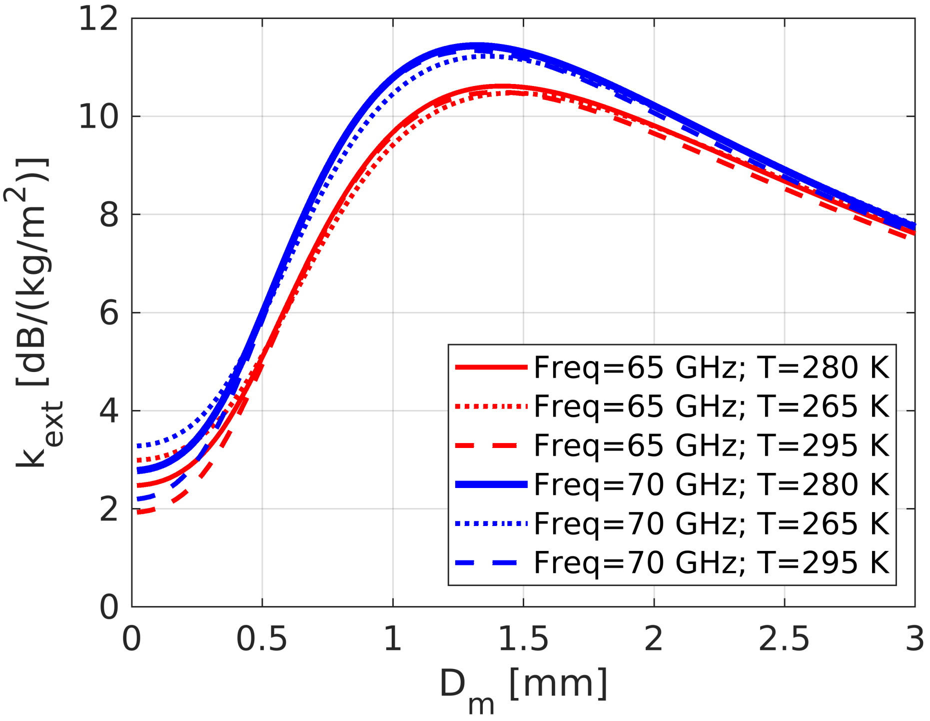

Figure 8. Extinction coefficients of rain as a function of the mean mass diameter for different temperatures at 65 and 70 GHz, i.e. in the frequency range practically available for the pressure technique in the right wing of the Oxygen line. An exponential drop size distribution is assumed.

For large liquid water paths this attenuation will produce a significant drop in the level of the signal (i.e. it will reduce SNR_o) but it will also cause some differential signal as shown in Fig. 9. The amplitude of the differential attenuation signal increases linearly with the separation of the tones and it is also a strong function of D_m for any given integrated liquid content. For a separation between tones of 5 GHz in the worst scenario ($D_m = 1.0$mm) 25 g/m^2 can cause a two-way differential attenuation of 0.06 dB which is expected to produce a bias of the order of few hPa according to the pressure sensitivity.

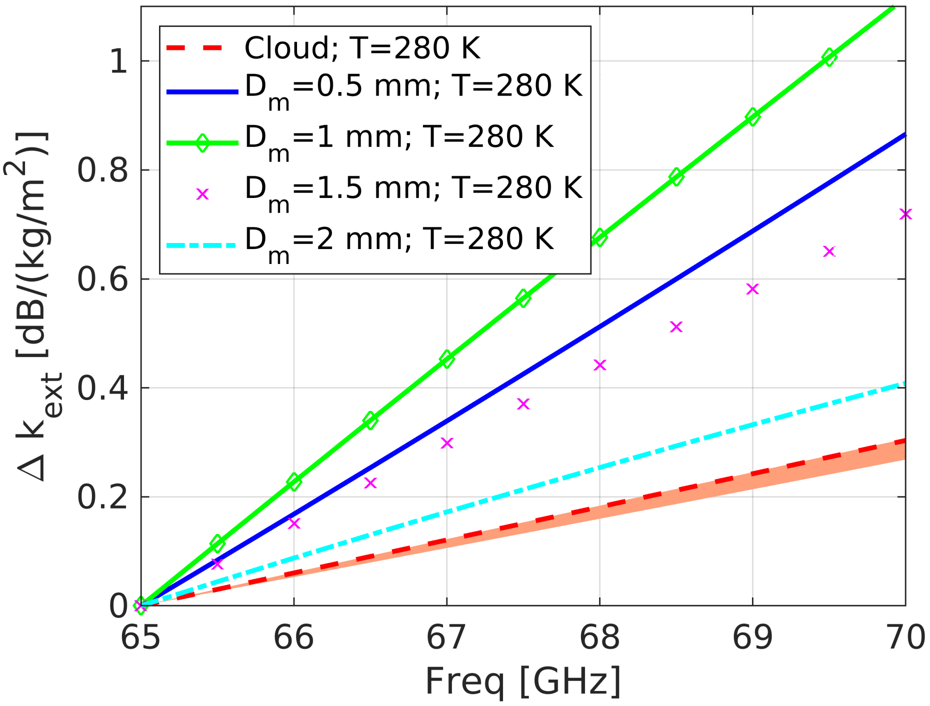

Figure 9. Differential extinction coefficients of rain as a function of frequency in the right wing of the Oxygen line for a temperature of 280 K and for different mean mass-weighted diameters as indicated in the legend. An exponential drop size distribution is assumed. For cloud the shading corresponds to temperature of 275 K (295 K) for the upper (lower) boundary.

For rain, the fact that the differential extinction signal depends both on the rain water path and on D_m make corrections quite tricky. The importance of the impact of the drop size distribution of rain was also found in the study by Millán et al. (2014). Also the overall signal can be up to five times bigger than cloud, with the same amount of integrated liquid path. Viceversa for clouds (see red curves in Fig. 9) corrections are simpler because there is only a slight dependence on temperature. Errors in the retrieved cloud water path up to 50 g/m^2 seem acceptable. In fact the increase of cloud extinction coefficient when moving from 65 to 70 GHz is of the order of 0.25 dB/(kg/m^2) which produce a 2-way attenuation of 0.025 dB when encountering a LWP=50 g/m^2.

Cloud and rain must be identified and flagged. Then only if we can achieve retrieval with uncertainties smaller than 50 g/m^2 for cloud and less than 25 g/m^2 for rain the differential absorption signal can be corrected; otherwise pressure retrievals will be very uncertain with large biases. Such estimates could be achieved via a multi-frequency radiometer. An alternative approach to better correct for these effects is to adopt a triple-tone approach (see discussion in Sect. 7).

The effect of ice differential attenuation is certainly more negligible as shown in Fig. 10.

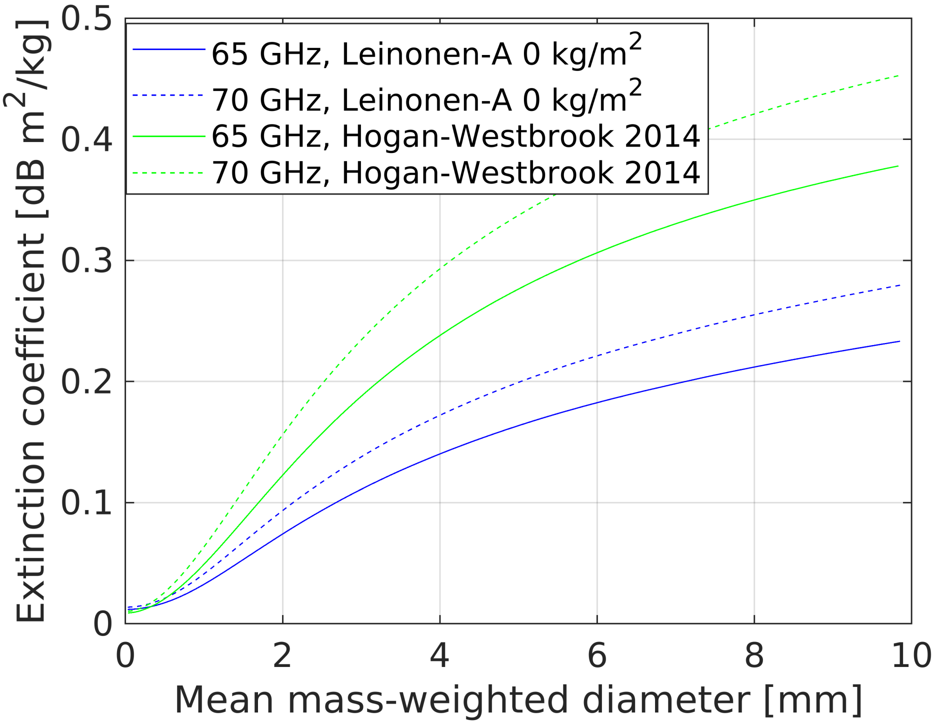

Figure 10. Extinction coefficients for ice clouds for two frequencies (65 and 70 GHz) and for two different model of ice scattering (fluffy aggregate from Leinonen et al. (2017) and denser ice from Hogan and Westbrook (2014)) as described in Tridon et al. (2019).

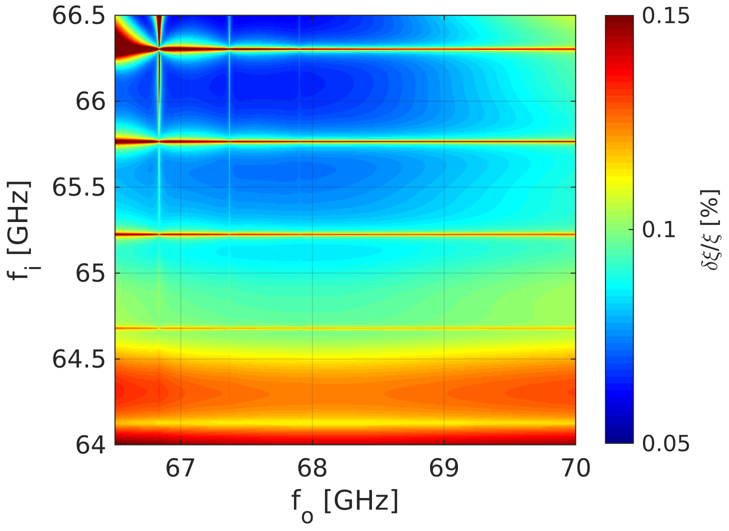

Figure 11. Relative uncertainty in the ξ quantity for temperature perturbations of 1.5 K (1-sigma) on the right wing of the O_2 line for a US-standard atmosphere.

3.5 Uncertainties in pressure sensitivity parameter

The last error source to consider is the one associated with the surface pressure sensitivity, $\xi(f_i, f_o)$. Uncertainties in the temperature profile are the main drivers of uncertainties in $\xi(f_i, f_o)$. Fig. 11 shows the impact of a 1.5 K (one sigma) temperature perturbations. The relative errors remain of the order of 1‰for typical frequency pair selections (which is in line with few hPa precision target).

4 Considerations for the design of a space-borne system

4.1 Spaceborne simulator

In order to provide an idea about the performances of a pressure DAR system we have developed a space-borne simulator. The simulator follows the logic implemented in Battaglia and Kollias (2019): orbits of the CloudSat satellite and the A-Train (sun-synchronous, polar, local time 2 AM) are used to sample the natural variability over a variety of surface, temperature, water vapor, hydrometeor conditions. The CloudSat 94 GHz (3.2 mm) Cloud Profiling Radar (CPR, Tanelli et al. (2008)) in combination with the CALIOP lidar of CALIPSO and the MODIS radiometer in the A-Train provide global observations of ice, rain and cloud profiles via the CAPTIVATE algorithm (Mason et al. (2022)) at a vertical resolution of 60 m and an along-track horizontal resolution of 1.5 km. Three classes of hydrometeors are retrieved: ice, cloud and rain with mass contents for all and characteristic sizes only for ice and rain. ECMWF auxiliary data are used as input for temperature, pressure and relative humidity, thus allowing the computation of gas attenuation. These profiles can be used to produce single scattering properties (backscattering and extinction), hence radar profiles.

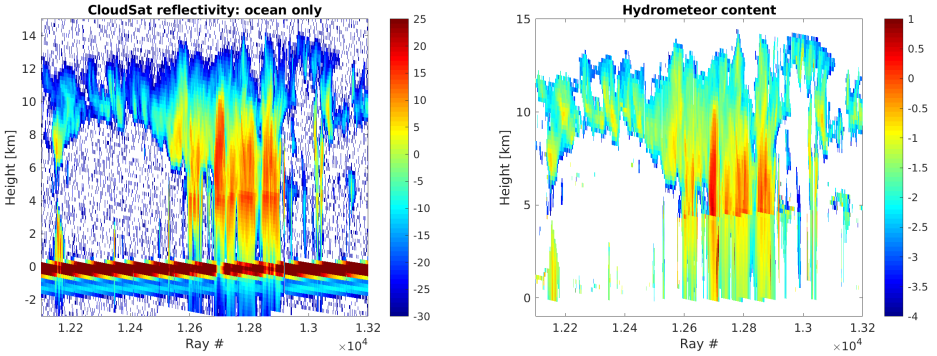

Figure 12. Detail of the CloudSat reflectivity in dBZ (left panel) and corresponding hydrometeor contents as retrieved from the CAPTIVATE algorithm (right panel) for a stratiform system.

An example of a stratiform system over ocean is shown in Fig. 12. The CloudSat reflectivity and the CAPTIVATE retrieved hydrometeor contents (where we have added up cloud, ice and rain contents) are depicted in the left and right panel, respectively. Different cloud systems are encountered during the orbit with different depths and equivalent water path amounts.

The simulation of two channels in the right wing of the 60 GHz band at 65.6 and 70 GHz is shown in Fig. 13. The reflectivity at 70 GHz resembles the one from CloudSat at 94 GHz, with less attenuation in the rain layer thanks to the smaller frequency. On the other hand the impact of moving toward the center of the oxygen absorption line is pretty obvious when looking at the simulation at 65.6 and 66 GHz (top and centre pan-

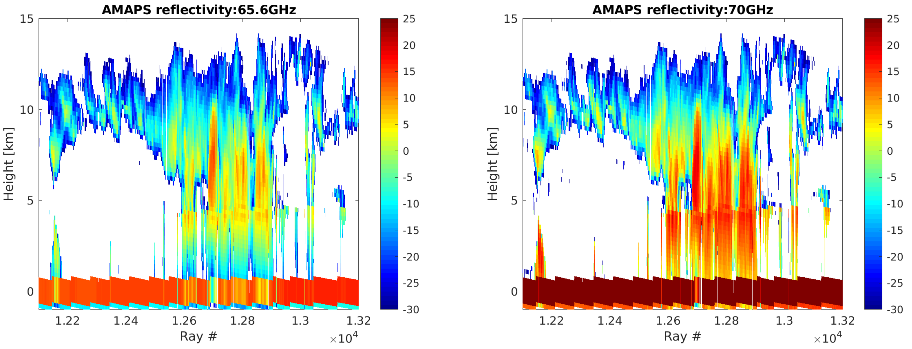

Figure 13. Simulation of reflectivities for an AMAPS radar with frequency at 65.6 and 70 GHz in correspondence to the scene shown in Fig. 12. A pulse width of 3.3 μs is assumed.

els) with increased levels of path integrated attenuation when going toward the surface. The surface returns also show a stark reduction when decreasing the frequency.

When considering all possible scenarios sampled by a polar orbiting satellite like CloudSat the cumulative pdf of cloud, rain and total (cloud+rain) liquid water path is obtained (left panel of Fig. 14). The pdf of SNR_o for a spaceborne radar with the specifics of Tab. 1 is shown in the right panel. For more than 90% of the time it exceeds 45 dB and it is basically bounded between 40 and 60 dB. These values certainly consent to substantially reduce the errors associated to the reflectivity measurement noisiness (Sect. 3.1).

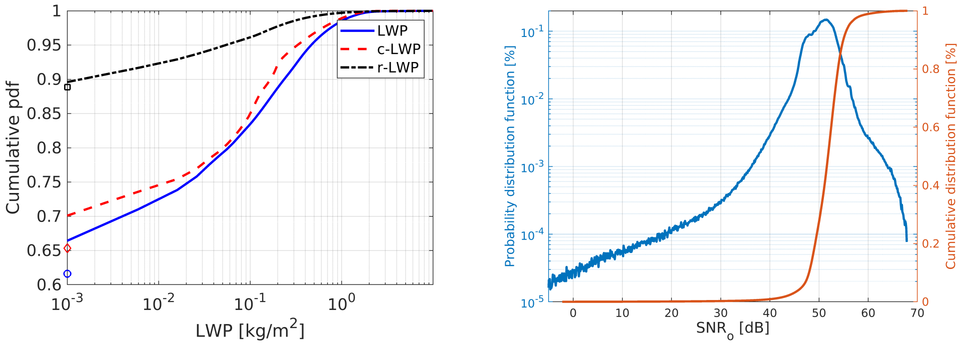

Figure 14. Left panel: cumulative PDF for the cloud, rain and total LWP Right panel: distribution and cumulative distribution of SNR_o (a 70 GHz channel has been assumed). The specs of Tab. 1 for the pressure mode have been used. The full 2008 year CloudSat dataset over the ocean has been used to build the statistics for both panels.

4.2 Number of independent samples

The number of independent samples, N is a critical quantity to achieve the targeted precision in the differential absorption signal between two tones (see Eq. 9), with reflectivity uncertainties decreasing with $\sqrt{N}$. Therefore longer integration times mean more independent samples and therefore better estimation accuracy but also poorer spatial resolution. For moving platforms in Low Earth Orbits the decorrelation between pulses is mainly driven by the satellite motion (more than by the intrinsic decorrelation of the ocean surface that at the selected wavelengths of about 4-6 mm can be as long as 4-12 ms in presence of calm sea). Independent samples are collected when the platform moves by approximately half the antenna diameter, D, i.e. the time to decorrelation or to independence, τ_i is given by Meneghini and Kozu (1990) as:

$$\tau_i = 0.48\frac{D}{v_{sat}} \tag{13}$$

With $D = 2$ m and $v_{sat} \approx 7.6$ km/s (orbit at 500 km height) this gives a decorrelation time of the order of 130 μs. Therefore, for all PRF lower than 8 kHz, successive pulses will tend to be decorrelated. So potentially a PRF=8 kHz produces 1,143 independent sample per km of integration length.

A PRF of 8 kHz gives an unambiguous range of 18.7 km. Increasing the PRF can be troublesome because second trip echoes (Battaglia, 2021) (e.g. coming from low reflecting ice clouds) can fold into the surface return and bias the estimate of the surface reflectivity. This is particularly relevant for the inner tone, for which the surface return will be dimmed because of the strong O_2 attenuation occurring in the lower layers. A biases lower than 0.01 dB corresponds in linear units to a relative change of about 0.2%, which will be caused by a target with a reflectivity -27 dB lower than the surface return. For a pulse length of 1 μs the inner tone reflectivity peak is expected to be 5-10 dB above the single pulse sensitivity (i.e. between 0 and 5 dBZ) so very tenuous ice clouds (between -27 and -22 dBZ) can cause biases. Therefore it is recommended to keep the PRF to values lower than 6 kHz (and unambiguous ranges higher than 25 km). This produces 857 independent samples per km of alont track integration. Instead of increasing the PRF, frequency diversity could be used to transmit more pulses and avoid second trip echoes (Meneghini & Kozu, 1990).

4.3 Pulse length

In general a longer (shorter) pulse requires smaller (larger) receiver bandwidth. Increasing the pulse length and reducing the receiver bandwidth to match the inverse of the pulse length has the advantage of improving the radar sensitivity to hydrometeors but for surface SNR there is no impact associated to selection of the pulse length if the same amount of energy is transmitted for any given pulse (i.e. the peak power is inversely proportional to the pulse length). On the other hand shorter pulses have the advantages of increasing the surface to hydrometeor ratio (see discussion in App. C). This will curb possible biases introduced by low level cloud and precipitation contamination and by second trip echoes; in addition shorter pulses are conducive to lower duty cycles.

4.4 Tone selection

The tone selection must be driven by different consideration:

- try to maximise pressure sensitivity (Fig. 3) but at the same time keep the tone as close as possible to minimize the impact of spectral variability of σ_0 and differential attenuation due to cloud and rain (and water vapor). Ceteris paribus (e.g. with the same PRF) the first priority to achieve better performances is to improve SNR. This is accomplished by producing the highest possible energy per pulse. With the same SNR, shorter pulses are preferable because there will be less contamination associated to low level clouds and precipitation.
- avoid ITU-prohibited regions. Currently the only bands allocated for active transmissions are between 65 and 66 GHz and near 78 GHz. The band between 65 and 66 GHz is very favorable because as demonstrated in Fig. 4 it coincides with the optimal inner frequency selections for the characteristic SNR_o values. Ideally the outer frequency should not be higher than 70 GHz because the error associated

to the surface reflectivity measurement does not decrease for higher values (Fig. 5) whereas all other errors are proportional to $f_0 - f_i$.

- Avoid secondary absorption lines at about 64.68, 65.22, 65.76, 66.30 GHz (see Fig. 2) that are more sensitive to temperature errors (Fig. 11).

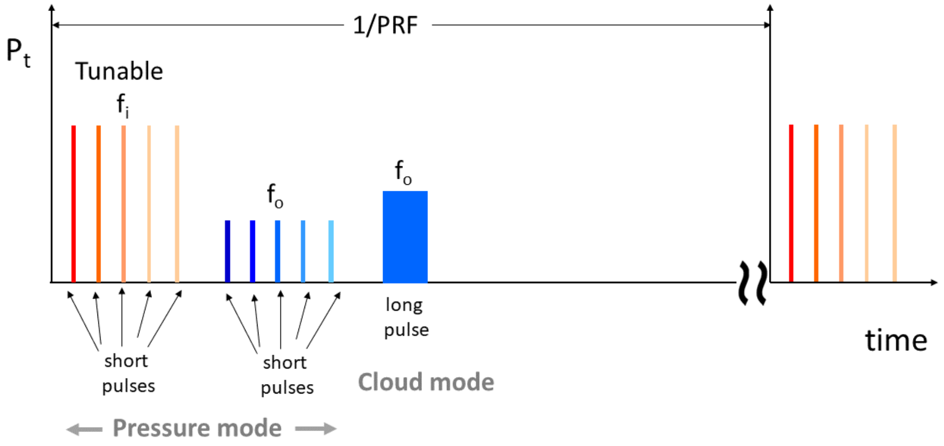

Figure 15. Pulse sequence for a DAR system with a pressure mode consisting of two trains of frequency-diverse short pulses around f_i and f_o and a cloud/precipitation mode with a single long pulse at f_o. For this configuration five different frequencies slightly different from f_i and f_o are envisaged.

One proposed pulse scheme for a DAR system is3illustrated in Fig. 15. The radar has a “pressure” and a “cloud” mode characterised by short (e.g. $1\,\mu s$) and long (e.g. $3.3\,\mu s$) pulses. The longer pulse in fact has the advantage of improving by roughly ($2\times 5.2 = 10.4$ dB) the hydrometeor sensitivity of the system.

In order to increase the number of independent samples frequency diversity is adopted in the pressure mode around both the inner and the outer frequency. The different coloured tones should be only separated by few MHz. Ideally the inner frequency should be tunable in order to optimize the precision of the differential radar reflectivities (as discussed in Sect. 3.1). Also it can be advantageous to try to balance the different channels in terms of SNR by sending more power to the inner than to the outer tones.

Similarly to what already suggested in the past (Kollias et al., 2007), an interlaced (“cloud”) mode with longer pulse duration should be envisaged to profile clouds and precipitation. This could be particularly effective for flagging rain contaminated profiles (drizzles occur at reflectivities larger than -20/-15 dBZ, Liu (2008)) and weaker echoes high in the troposphere that, when folded, could produce harmful biases.

5 Conclusions and recommendations

We summarize some of the key findings of this study.

- AMAPS systems that uses the differential signal of the surface return from tones inside the O_2 absorption band have great potential to retrieve the surface pressure with errors of the order of few hPa. Because such errors correspond to uncertainties of the order of few ‰, the AMAPS measurements require a tight control of all potential sources of errors.

- There are random and systematic errors associated to the AMAPS measurements linked to the different terms that appear in Eq. (7).
    1. Uncertainties in the temperature profile are the main error sources for the pressure sensitivity term $\xi(f_i, f_o)$. Typically temperature profiles must be known within 1K (random errors) to be able to estimate $\xi(f_i, f_o)$ within few ‰. Uncertainties in temperature profiles can be more severe inside clouds and precipitation because of the presence of latent heat release and radiative effects. Therefore such conditions may be more challenging than clear sky conditions.
    2. Water vapour differential attenuation signal shall be estimated and corrected. Random and biases on IWV contents will translate into errors in pressure estimate. Example of how uncertainties in IWV propagates into uncertainties of pressure are shown in Fig. 7. Again estimates of IWP are more uncertain in presence of clouds and precipitation.
    3. Cloud and precipitation contribute to differential attenuation; even in presence of 50 and 100 g/m^2 columnar contents of rain and cloud, respectively, biases in pressure estimates of the order of few hPa are expected. To minimize the biases the different tones of the DAR should be selected as close as possible, compatibly with pressure sensitivity. The impact of rain can be up to 5 times bigger than cloud for the same amount of columnar water and it is strongly dependent on the DSD details. Methodologies to flag the presence of rain and cloud should be developed. Otherwise differential attenuation corrections could be developed based on methods capable of estimating cloud liquid water path for cloud only and of rain liquid water path and characteristic sizes for rain only or both in presence of cloud and rain.

       If three tones are available it is possible to use the extra tone to estimate and correct for the impact of the hydrometeor differential attenuation. The methodology seems to work very well for cloud conditions; in presence of rain the correction deteriorates at large rain water paths (exceeding 1 kg/m^2). Such situations can be easily flagged.
    4. The variability of σ_0 with frequency also contribute to the overall error. Again this error, like 2. and 3. will increase with the separation between the channels and Fresnel models can be used to mitigate biases introduced by this effect. Such corrections should bring errors in surface pressure well below the hPa value. More studies are recommended to understand if the correction based on formula (10) can actually achieve such level of errors.
- The selection of the optimal frequency pair is driven by the SNR_o, i.e. the signal to noise ratio that would be measured in the outer band. Such level depends on the radar sensitivity and on the specific scene under observation (water vapor and hydrometeors cause attenuation). If SNR_o is quite large then the in-band channel can be positioned closer to the band centre. Ideally this selection could be adaptive if the system had the possibility of changing the inner frequency in a spectral band (e.g. between 65 and 66 GHz).
- The first priority to improve AMAPS SNR, thus its performances, should be to produce the highest possible energy per pulse. Pulse compression could be useful in this framework. With the same SNR shorter pulses are preferable because there will be less contamination associated to low level clouds and precipitation. An interlaced mode with longer pulse duration should be envisaged to detect and flag precipitation and to profile clouds, especially if high PRF (thus short unambiguous ranges) are foreseen.
- To reduce the uncertainties in the reflectivity estimates it maybe potentially useful to increase the number of samples, thus, with the same amount of mean transmitted power, to operate at high duty cycles, in other words to trade-off SNR with

number of pulses. However high PRF may be extremely dangerous for second trip echoes biasing the surface signal. Solutions like frequency diversity should be explored to be able to collect a sufficient number of pulses for achieving the required precision. This balance between SNR and number of pulses needs to be carefully studied for each ad-hoc configuration.

6 Appendix A: estimation of surface signal error

In general the voltage at the input detector is the sum of the contributions from the surface and the system noise:

$$V_{tot} = V_{surf} + V_{noise} \tag{14}$$

Assuming that the in-phase (in-quadrature) components of V_{surf} and V_{noise} are uncorrelated zero-mean Gaussian random variables, the in-phase (in-quadrature) component of V_{tot} is also a zero-mean Gaussian with a variance equal to the sum of the variances of the in-phase (in-quadrature) components. An estimate of the power formed from N independent samples is:

$$\hat{P}_{tot} = \frac{1}{N}\sum_{i=1}^{N} V_{tot}[i]\, V^{\star}_{tot}[i] = \left(\bar{P}_{surf} + \bar{P}_{noise}\right)\, f_N \tag{15}$$

where $\bar{P}_{surf}$ and $\bar{P}_{noise}$ are the mean values of the surface and system noise powers and where the pdf of f_N is:

$$p(f_N) = \frac{N^N\, f_N^{N-1}}{(N-1)!}\exp(-N f_N). \tag{16}$$

To find the surface return power, P_{surf}, consider the estimate:

$$\hat{P}_{surf} = \hat{P}_{tot} - \hat{P}_{noise} \tag{17}$$

where the second term is the estimate of the noise derived by M independent samples in the absence of a surface signal.

An estimate of the quality of the estimate of P_{surf} is the ratio of its standard deviation, $\sigma(\hat{P}_{surf})$ and its mean estimate, $E(\hat{P}_{surf})$:

$$\frac{\sigma(\hat{P}_{surf})}{E(\hat{P}_{surf})} = \sqrt{\frac{1}{N}\left[\left(1+\frac{1}{SNR}\right)^2 + \frac{1}{SNR^2}\frac{N}{M}\right]} = \frac{1}{SNR}\sqrt{\frac{1}{N}}\sqrt{(1+SNR)^2 + \frac{N}{M}} \tag{18}$$

where $SNR = \frac{\hat{P}_{surf}}{\hat{P}_{noise}}$ is the signal-to-noise per pulse. In general we expect that $M \gg N$ because we can get many more independent samples of the noise so that Eq. (18) becomes:

$$\frac{\sigma(\hat{P}_{surf})}{E(\hat{P}_{surf})} \approx \sqrt{\frac{1}{N}}\left(1+\frac{1}{SNR}\right) \tag{19}$$

7 Appendix B: triple tone approach

Hydrometeor can be very detrimental for AMAPS. This is illustrated in Fig. 16 which shows that the ΔPIA_{hydro} can reach almost 2 dB for the pair (65,70) GHz. With closer frequencies the result is expected to scale with frequency difference. It is clear that the differential attenuation tends to increase with the LWP but with two different modes: a cloud mode and a rain mode (they correspond to the lower and upper clusters in Fig. 16). This makes the correction utterly difficult, because not only the LWP but also the partitioning between cloud and rain must be determined.

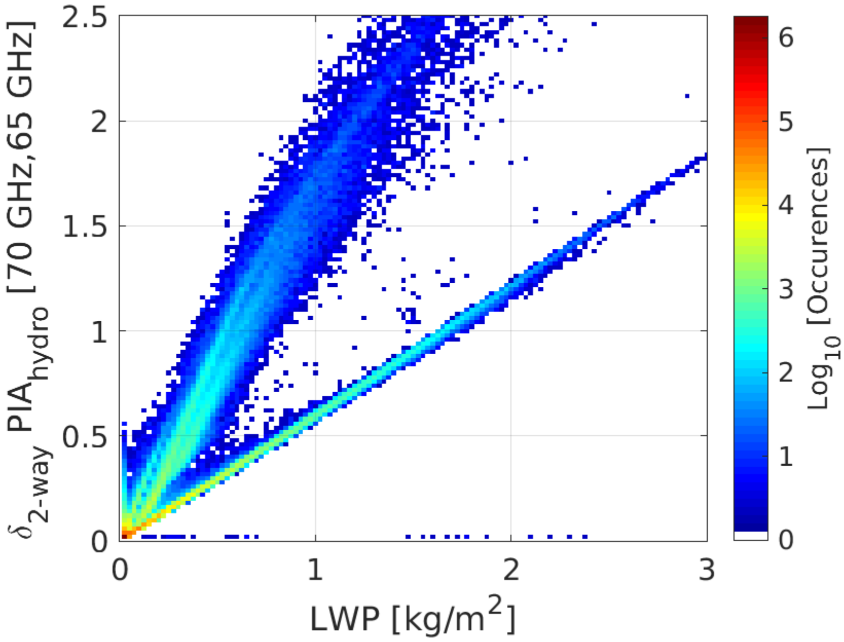

Figure 16. Density plot for the differential two-way PIAs caused by hydrometeors for the 65-70 GHz pair as a function of the total liquid water content. CloudSat profiles over ocean have been considered where the 2C- product is available (i.e. profiles with extremely high precipitation are excluded).

A different approach is here propose that uses at least a triplet of frequencies. With such measurements it is possible to write a system of equations :

$$\Delta Z_{surf}(f_o,\ f_i) - \Delta\sigma_0(f_o,\ f_i) = \xi(f_i,\ f_o)\, p_{surf} + 40\log_{10}\left[\frac{f_i}{f_o}\right] - \Delta_2[PIA_{hydro} + PIA_{wv}](f_o,\ f_i) \qquad (20)$$

$$\Delta Z_{surf}(f_o,\ f_m) - \Delta\sigma_0(f_o,\ f_m) = \xi(f_m,\ f_o)\, p_{surf} + 40\log_{10}\left[\frac{f_m}{f_o}\right] - \Delta_2[PIA_{hydro} + PIA_{wv}](f_o,\ f_m) \qquad (21)$$

where the hydrometeor effect can be eliminated in this system under the assumption that the differential PIA is linearly proportional to the frequency difference, i.e.:

$$\Delta_2 PIA_{hydro}(f_i,\ f_j) \propto \Delta f = \gamma_{i,j}(c-LWP, r-LWP)\Delta f \qquad (22)$$

where the term $\gamma(c-LWP, r-LWP)$ will depend on the LWP and the partitioning between rain (r-LWP) and cloud (c-LWP) but very slightly on the frequency. Of course this assumption is more and more valid when considering narrower and narrower range of tone frequencies. By dividing Eqs.(20-21) by $\Delta f_{i,o}$ and $\Delta f_{m,o}$:

$$\frac{\Delta Z_{surf}(f_o,\ f_i)}{f_o - f_i} = \frac{\xi(f_i,\ f_o)}{f_o - f_i}\, p_{surf} - \gamma_{i,o} + A(f_i,\ f_o,\ IWP,\ \sigma_0) \qquad (23)$$

$$\frac{\Delta Z_{surf}(f_o,\ f_m)}{f_o - f_m} = \frac{\xi(f_m,\ f_o)}{f_o - f_m}\, p_{surf} - \gamma_{m,o} + B(f_o,\ f_m,\ IWP,\ \sigma_0) \qquad (24)$$

where A and B include the water vapor and σ_0 corrections and the frequency scaling factors. By subtracting Eq. (24) from Eq. (23) γ will practically cancel out and p_{surf} will be determined as:

$$p_{surf} = \frac{\frac{\Delta Z_{surf}(f_o, f_i)}{f_o - f_i} - \frac{\Delta Z_{surf}(f_o, f_m)}{f_o - f_m} - A(f_i,\ f_o,\ IWP) + B(f_o,\ f_m,\ IWP) + \gamma_{i,o} - \gamma_{m,o}}{\frac{\xi(f_i, f_o)}{f_o - f_i} - \frac{\xi(f_m, f_o)}{f_o - f_m}} \qquad (25)$$

from the measurements of the surface reflectivities at the three tones.

The cancellation between the two terms $\gamma_{i,o}$ and $\gamma_{m,o}$ caused by hydrometeor PIA works well. The residuals

$$\eta \equiv \gamma_{m,o} - \gamma_{i,o} = \frac{\Delta PIA_{hydro}(f_o,\ f_m)}{f_o - f_m} - \frac{\Delta PIA_{hydro}(f_i,\ f_o)}{f_o - f_i} \tag{26}$$

are generally small. In Fig. 17 we show the result for the triplet 65, 66 and 70 GHz. The term at the denominator of Eq. (25) is of the order of 0.02 dB/(hPa GHz) for the triplet 65, 66 and 70 GHz. The two branches correspond to cloud (horizontal one) and rain (descending one). This means that, if Eq. (25) is used, biases introduced by cloud and rain are less than 0.5 hPa certainly for cloudy and rainy conditions with LWP less than 1 kg/m^2.

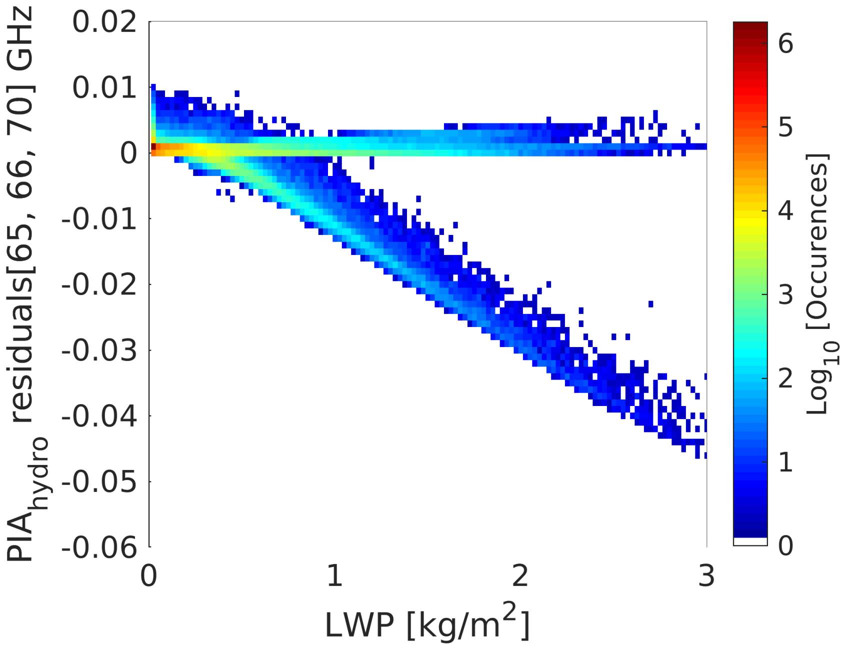

Figure 17. Density plot for the residuals in PIAs in dB/GHz (see Eq. 26) caused by hydrometeors for the 65-66-70 GHz triplet as a function of LWP.

As a rule of thumb, because of the amplitude of the differential attenuation signal certainly in situations with LWP exceeding 2 kg/m^2 it will be very tricky to correct for hydrometeor attenuation. This situation will be very easy to flag because the impact of such hydrometeor will exceed 8 dB in the two way attenuation (see Fig. 8). Rain with LWP exceeding 2 kg/m^2 is easy to flag due to its intermittant signal.

8 Appendix C: impact of pulse scheme on surface and hydrometeor SNR and number of samples

Pulse compression methods are known to be useful for increasing the number of independent samples and avoid high peak powers. Let's assume that the desired resolution is Δr (e.g. 100 m). If we used a quasi-monochromatic pulse then $\Delta r = c\tau/2$. With pulse compression, with a pulse of duration τ' and a modulated frequency with bandwidth B' an effective range resolution $\Delta r' = c/(2B')$ can be achieved with a pulse compression gain $G_{pc} = B'\tau'$.

Table 2. Impact of the pulse scheme (quasi-monochromatic vs pulse compression) on SNR for hydrometeor and surface targets.

Quantity	Monochromatic pulse	Pulse compression
Transmitted power	P_t	P'_t
Pulse length	τ	τ'
Pulse energy	$P_t\tau$	$P'_t\tau'$
Noise figure	F	F'
Resolution	$c\tau/2$	$c/(2B')$
HYDROMETEORS		
Signal	$Z_{hydro} \propto P_t\tau$	$Z'_{hydro} \propto P'_t\tau'$
Noise	$Z_{noise} \propto BF$	$Z'_{noise} \propto B'F'$
Signal to noise ratio	$SNR \propto \frac{P_t\tau}{BF}$	$SNR' \propto \frac{P'_t\tau'}{B'F'}$
SURFACE		
Signal	$Z_{surf} \propto P_t$	$Z'_{surf} \propto P'_t B'\tau'$
Noise	$Z_{noise} \propto BF$	$Z'_{noise} \propto B'F'$
Signal to noise ratio	$SNR \propto \frac{P_t}{BF}$	$SNR' \propto \frac{P'_t\tau'}{F'}$

A pulse compression system transmitting a power P'_t for a duration τ' is equivalent to a monochromatic pulse of peak power $P'_T B'\tau'$ and duration $1/B'$ (Meneghini & Kozu, 1990). This allows to compute the expected amplitude of the surface and hydrometeor reflectivity returns (see Tab. 2). For atmospheric targets, with pulse compression, for a desired range resolution Δr s an increase in independent samples equal to:

$$m = \frac{\Delta r}{\Delta r'} = \tau B' = G_{pc}\frac{\tau}{\tau'} = G_{pc}$$

is obtained if τ' is matched to τ. But no improvement in the number of samples is obtained for the surface return. However, this has a drawback on the SNR per pulse. If the average power transmitted remains constant ($P_t\tau = P'_t\tau'$) and if the noise figures F and F' are the same in the two configurations then $(SNR/SNR')_{hydro} = m$ and $(SNR/SNR')_{surf} = 1$.

Therefore the increased number of samples in the pulse compressed signal is compensated by a decrease of the same factor in SNR for atmospheric targets but there is no practical change if surface return is the required measurement; pulse compression is really beneficial because it allows to send power with smaller peak power. Frequency diversity on the other hand allows to trade-off number of independent pulses over single pulse SNR.

Acknowledgments

This research has been supported by the European Space Agency (ESA) that has funded the feasibility study (ESA Contract number: 4000120263/17/NL/FE) as well as the design of an airborne demonstrator of the Active Microwave Air Pressure Sensor (AMAPS) (ESA Contract No. 4000140192/22/NL/AS) led by RAL Space. The AMAPS sensitivity study (Contract ESA-TRP-TECEFP-SOW-022520) led by Politecnico di Torino. The authors would also like to thank the Science and Technology Research Council (UKRI/STFC) and the Centre of Earth Observation Instrumentation for funding the design of the first two channel demonstrator and the triple channel demonstrator respectively. (ESA Contract Number 4000136466/21/NL/LF) and “End-to-End Performance Simulator Activity of the WIVERN Mission" (ESA Contract Number 4000139446/22/NL/SD). This research used the Mafalda cluster at Politecnico di Torino.

References

Battaglia, A. (2021). Impact of second-trip echoes for space-borne high-pulse-repetition-frequency nadir-looking w-band cloud radars. *Atm. Meas. Tech.*, *14*(12), 7809–7820. Retrieved from `https://amt.copernicus.org/articles/14/7809/2021/` doi: 10.5194/amt-14-7809-2021

Battaglia, A., & Kollias, P. (2019). Evaluation of differential absorption radars in the 183 GHz band for profiling water vapour in ice clouds. *Atm. Meas. Tech.*, *12*(6), 3335–3349. Retrieved from `https://www.atmos-meas-tech.net/12/3335/2019/` doi: 10.5194/amt-12-3335-2019

Battaglia, A., Kollias, P., Dhillon, R., Roy, R., Tanelli, S., Lamer, K., … Furukawa, K. (2020). Spaceborne cloud and precipitation radars: Status, challenges, and ways forward. *Reviews of Geophysics*, *58*(3), e2019RG000686. Retrieved from `https://agupubs.onlinelibrary.wiley.com/doi/abs/10.1029/2019RG000686` (e2019RG000686 10.1029/2019RG000686) doi: 10.1029/2019RG000686

Battaglia, A., Wolde, M., D'Adderio, L. P., Nguyen, C., Fois, F., Illingworth, A., & Midthassel, R. (2017). Characterization of Surface Radar Cross Sections at W-Band at Moderate Incidence Angles. *IEEE Trans. Geosci. Remote Sens.*, *55*(7), 3846-3859. (10.1109/TGRS.2017.2682423)

Flower, D., & Peckham, G. E. (1978). *A microwave pressure sounder* (Tech. Rep.). JPL Publication 78-68, Caltech.

Hogan, R. J., & Westbrook, C. D. (2014). Equation for the microwave backscatter cross section of aggregate snowflakes using the self-similar rayleigh-gans approximation. *J. Atmos. Sci.*, *71*, 3292-3301.

Kollias, P., Szyrmer, W., Zawadzki, I., & Joe, P. (2007). Considerations for spaceborne 94 GHz radar observations of precipitation. *Geophys. Res. Lett.*, *34*(21). Retrieved from `https://agupubs.onlinelibrary.wiley.com/doi/abs/10.1029/2007GL031536` doi: 10.1029/2007GL031536

Lebsock, M. D., Suzuki, K., Millán, L. F., & Kalmus, P. M. (2015). The feasibility of water vapor sounding of the cloudy boundary layer using a differential absorption radar technique. *Atm. Meas. Tech.*, *8*(9), 3631–3645. Retrieved from `https://www.atmos-meas-tech.net/8/3631/2015/` doi: 10.5194/amt-8-3631-2015

Leinonen, J., Kneifel, S., & Hogan, R. J. (2017). Evaluation of the Rayleigh-Gans approximation for microwave scattering by rimed snowflakes. *Quart. J. Roy. Meteor. Soc.*, *144*(S1), 77-88. doi: 10.1002/qj.3093

Li, L., Heymsfield, G. M., Tian, L., & Racette, P. E. (2005). Measurements of Ocean Surface Backscattering Using an Airborne 94 GHz Cloud Radar- Implication for Calibration of Airborne and Spaceborne W-Band Radars. *J. Atmos. Ocean Technol.*, *22*(7), 1033-1045. (DOI: http://dx.doi.org/10.1175/JTECH1722.1)

Liebe, H., Rosenkranz, P., & Hufford, G. (1992). Atmospheric 60-ghz oxygen spectrum: New laboratory measurements and line parameters. *J. Quant. Spectrosc. Radiat. Transfer*, *48*(5), 629-643. Retrieved from `https://www.sciencedirect.com/science/article/pii/002240739290127P` (Special Issue Conference on Molecular Spectroscopic Databases) doi: https://doi.org/10.1016/0022-4073(92)90127-P

Lin, B., & Hu, Y. (2005). Numerical simulations of radar surface air pressure measurements at o_2 bands. , *2*(3), 324-328. doi: 10.1109/LGRS.2005.848515

Lin, B., & Min, Q. (2017). Optimal frequency selection of multi-channel o2-band different absorption barometric radar for air pressure measurements.

J. Quant. Spectrosc. Radiat. Transfer, *188*, 188-191. Retrieved from `https://www.sciencedirect.com/science/article/pii/S0022407316300565` (Advances in Atmospheric Light Scattering: Theory and Remote Sensing Techniques) doi: https://doi.org/10.1016/j.jqsrt.2016.06.019

Lin, B., Min, Q., & Hu, Y. (2021). Assessing surface air pressure sensing using 118 ghz o2-absorption radar system. *J. Quant. Spectrosc. Radiat. Transfer*, *261*, 107425. Retrieved from `https://www.sciencedirect.com/science/article/pii/S0022407320309535` doi: https://doi.org/10.1016/j.jqsrt.2020.107425

Liu, G. (2008). A database of microwave single-scattering properties for nonspherical ice particles. *Bull. Amer. Met. Soc.*, *89*, 1563-1570.

Mason, S., Hogan, R. J., Bozzo, A., & Pounder, N. (2022). A unified synergistic retrieval of clouds, aerosols and precipitation from earthcare: the acm-cap product. *Atm. Meas. Tech.*, *to be submitted*.

Meneghini, R., & Kozu, T. (1990). *Spaceborne weather radar.* Artech House.

Millán, L., Lebsock, M., Livesey, N., & Tanelli, S. (2016). Differential absorption radar techniques: water vapor retrievals. *Atm. Meas. Tech.*, *9*(6), 2633–2646. Retrieved from `https://www.atmos-meas-tech.net/9/2633/2016/` doi: 10.5194/amt-9-2633-2016

Millán, L., Lebsock, M., Livesey, N., Tanelli, S., & Stephens, G. (2014). Differential absorption radar techniques: surface pressure. *Atm. Meas. Tech.*, *7*(11), 3959–3970. Retrieved from `https://amt.copernicus.org/articles/7/3959/2014/` doi: 10.5194/amt-7-3959-2014

Roy, R. J., Lebsock, M., Millan, L., Dengler, R., R., R. M., Siles, J. V., & Cooper, K. B. (2018). Boundary-layer water vapor profiling using differential absorption radar. *Atm. Meas. Tech.*, *11*, 6511-6523. (doi: 10.5194/amt-11-6511-2018)

Roy, R. J., Lebsock, M., Millán, L., & Cooper, K. B. (2020). Validation of a G-band differential absorption cloud radar for humidity remote sensing. *J. Atmos. Ocean Technol.*. Retrieved from `https://doi.org/10.1175/JTECH-D-19-0122.1` doi: 10.1175/JTECH-D-19-0122.1

Schwartz, M. J. (1998). *Observation and modeling of atmospheric oxygen millimeter-wave transmittance* (Unpublished doctoral dissertation).

Tanelli, S., Im, E., Durden, S., Giuli, D., & Facheris, L. (2008). Spaceborne Doppler radars for atmospheric dynamics and energy budget studies. In IEEE (Ed.), *Radar conference* (p. 1-6). (10.1109/RADAR.2008.4721127)

Tridon, F., Battaglia, A., Chase, R. J., Turk, F. J., Leinonen, J., Kneifel, S., … Nesbitt, S. (2019). The Microphysics of Stratiform Precipitation During OLYMPEX: Compatibility Between Triple-Frequency Radar and Airborne In Situ Observations. *J. Geophys. Res. Atm.*, *124*(15), 8764-8792. Retrieved from `https://agupubs.onlinelibrary.wiley.com/doi/abs/10.1029/2018JD029858` doi: 10.1029/2018JD029858